Concrete Engineering   콘크리트공학

Effects of Matrix Strength, Fiber Type, and Fiber Content on the Electrical Resistivity of Steel-Fiber-Reinforced Cement Composites During Fiber Pullout

Le, Huy Viet*, Kim, Dong Joo**

Le, Huy Viet* · 김동주**

매트릭스 강도, 섬유 형식 및 보강량에 강섬유 보강 시멘트 복합재료의 인발시 전기저항에 미치는 영향

ABSTRACT

Development of smart construction materials with both self-strain and self-damage sensing capacities is still difficult because of little information about the self-damage sensing source. Herein, we investigate the effects of the matrix strength, fiber geometry, and fiber content on the electrical resistivity of steel-fiber-reinforced cement composites by multi-fiber pullout testing combined with electrical resistivity measurements. The results reveal that the electrical resistivity of steel-fiber-reinforced cement composites clearly decreased during fiber-matrix debonding. A higher fiber-matrix interfacial bonding generally leads to a higher reduction in the electrical resistivity of the composite during fiber debonding due to the change in high electrical resistivity phase at the fiber-matrix interface. Higher matrix strengths, brass-coated steel fibers, and deformed steel fibers generally produced higher interfacial bond strengths and, consequently, a greater reduction in electrical resistivity during fiber debonding.

Key words : Self sensing, Fiber matrix interface, Electrical resistivity, Multiple fiber pullout, Steel fiber reinforced cement composite

초 록

자가응력 및 자가손상 감지능력을 모두 가지는 스마트 콘크리트의 개발은 아직까지 손상 감지 능력에 대한 원인 규명이 명확하지 않아 어려운 현실이다. 따라서, 본 연구에서는 매트릭스 강도, 섬유 형식 및 보강량이 강섬유 보강 시멘트 복합재료의 인발시 전기저항에 미치는 영향을 평가하였다. 실험으로부터 섬유와 매트릭스 사이 계면에서의 탈착으로 전기저항률이 감소한다는 사실을 알 수 있었다. 섬유와 매트릭스 사이 계면 부착강도가 높을수록 더 큰 전기저항률의 감소를 유발하였다. 따라서, 고강도 매트릭스, 황동 도금된 강섬유 그리고 변형된 강섬유를 사용시 높은 계면부착강도를 유발하고 그 결과 더 큰 전기저항률 감소를 유발하였다.

검색어 : 자가감지, 섬유와 매트릭스 사이 계면, 전기저항률, 다수의 섬유인발, 강섬유보강 시멘트 복합재료

1. Introduction

There has been significant interest in the development of smart construction materials capable of self-sensing under external loads. Self-sensing capacities include self-strain sensing within the linear elastic limit of the material, as well as self-damage sensing, including

* 세종대학교 건설환경공학과, 박사 후 연구원 (Sejong University · lehuyviet.mdc@gmail.com)
** 정회원 · 교신저자 · 세종대학교 건설환경공학과, 교수 (**Corresponding Author** · Sejong University · djkim75@sejong.ac.kr)

matrix cracking, and the capacity to sense even beyond the elastic limit of the material. The smart concrete with self-damage and self-stress sensing abilities has great potential to apply for infrastructures such as high rise building, large span bridges, tunnels, and nuclear power plan (Han et al., 2014). Moreover, a potential application of smart concrete with self-damage sensing ability is underground structure like pipelines (Pour-Ghaz et al., 2011). To apply smart concretes for structural health monitoring system of infrastructures, the sensing gauge generally are apply to critical position of structure. For example, in case of a smart sensing structure with beam type, the sensing gauge generally can be put at the tensile zone of the middle of the beam to monitor damages or put at the compressive zone to monitor the stress. Most smart construction materials that contain electrically conductive fillers generally have shown self-strain sensing within the elastic limit, whereas a few researchers have recently reported self-damage or crack-sensing capacities beyond the limit by exploiting changes in electrical resistivity due to matrix cracking. However, it is still very difficult to develop a smart construction material capable of both self-strain and self-damage sensing.

The self-strain (or stress) sensing response of a smart construction material is mostly based on changes in the electrical resistivity of the material under an external load owing to mobile ions in its pore solution system and changes in the network of the electrically conductive filler within the material. The addition of conductive materials, such as carbon nanotubes (CNTs) (Han et al., 2009), multi-wall carbon nanotubes (MWCNTs) (Han et al., 2012; Yoo et al., 2017), graphene (Yoo et al., 2017), graphite nanofibers (Yoo et al., 2017), nickel (Han et al., 2011), steel fibers (Chung, 2002; Wen and Chung, 2003), carbon fibers (Fu et al., 1998; Shi and Chung, 1999; Bontea et al., 2000; Chung, 2002; Wen and Chung, 2003), or hybrid materials (Fu et al., 1998; Shi and Chung, 1999; Bontea et al., 2000; Chung, 2002; Wen and Chung, 2003), has been shown to enhance the conductive networks of the composites, resulting in improved self-sensing abilities. Table 1 summarizes the self-strain (or stress) sensing capacities of a variety of self-sensing cement-based materials in their elastic regions under external loads. The strain-sensing capacity is evaluated by determining the gauge factor (*GF*), which is the fractional change in electrical resistance per unit strain. Table 1 reveals that among several self-strain cement-based composites, steel-fiber-reinforced cementitious composites (SFRCs) produced the highest

values of *GF* under both compressive and tensile loads; the *GF* values of an SFRC under compression and tension were 720 and 4560, respectively (Wen and Chung, 2003).

On the other hand, macrofiber-reinforced cementitious composites, such as high-performance fiber-reinforced cementitious composites (HPFRCCs) with steel fibers, and engineered cementitious composites (ECCs) with polyvinyl alcohol (PVA) fibers, have recently been reported to exhibit self-damage sensing capacities. Ranade et al. (2014) reported the highest GF value of a PVA-fiber-containing ECC after matrix cracking under tension (*GF* = 232), as summarized in Table 1. The electrical resistivities of HPFRCCs containing steel fibers were observed to suddenly decrease with increasing numbers of cracks during their unique tensile-strain hardening responses that were accompanied by multiple microcracks (Nguyen et al., 2014; Song et al., 2015; Le and Kim, 2017; Kim et al., 2018). However, the electrical resistivities of the ECCs increased with increasing numbers of cracks (Hou and Lynch, 2005; Ranade et al., 2014). These different trends in electrical resistance following matrix cracking (i.e., the damage-sensing capacities) originate in the different interfacial characteristics of the materials, as well as the fibers used. However, there is little information on the effects of fiber-matrix interfacial characteristics on electrical resistivity during fiber pullout. Thus, a deep understanding of the effects of fiber-matrix interfacial characteristics on the electrical resistivities of fiber-reinforced composites is required in order to develop smart construction materials with both self-strain and self-damage sensing capacities.

In this study, we sought to gain a deeper understanding of the effects of fiber-matrix interfacial characteristics on the electrical resistivity of fiber-reinforced cement composites during fiber pullout. Since the properties of the matrix, the fiber geometry, and the fiber coating strongly influence the interfacial bond strength (Al Khalaf et al., 1980; Alwan et al., 1991; Naaman and Najm, 1991; Shannag et al., 1997; Bentur and Alexander, 2000; Chan and Chu, 2004; Kim et al., 2010), their effects on sensing capacity require careful investigation. In addition, the effect of the number of embedded fibers on sensing capacity also should be studied. The objectives of this study include investigating the effects of the matrix, fiber geometry, the fiber-coating material, and the number of fibers on the electromechanical responses of steel-fiber-reinforced cement composites during fiber pullout.

Table 1. Various Self-Sensing Cement Based Materials

No.	Sensing capacity	f'_c MPa	f_t MPa	GF compression	GF Tension	Functional filler	Fibers	Fiber vol %	Ref.
1	Stress					CNT			Han et al.(2009)
2	Stress					MWCNT			Han et al.(2012)
3	Strain	35.2		113.2		MWCNT			Yoo et al.(2017)
		35.2				Graphene			
		35.2				Graphite nanofiber			
4	Stress					Nickel			Han et al.(2011)
5	Strain			200±30	4560±640		Smooth steel	0.72	Wen and Chung(2003)
				720±100	1290±160		Smooth steel	0.36	
				350±30	90±10		Carbon	0.5	
6	Strain	14					Carbon		Fu et al.(1998)
7	Strain		1.97		625		Carbon		Bontea et al.(2000)
			1.97		700		Carbon treatment		
9	Strain, stress	40		227		CB	Carbon		Han and Ou(2007)
10	Strain			445		CNT	Carbon		Azhari et al.(2012)
11	Damage	90	10		138.1±35.7		Long twisted steel	1.5	Nguyen et al.(2014)
		90	7.54		99.9±9.1		Long smooth steel		
		90	6.72		88.5±25.7		Long hooked steel		
		90	11		139.7±28.3		Medium twisted steel		
		90	8.05		99.7±26.1		Medium smooth steel		
		90	5.69		52.9±4.0		Short smooth steel		
11	Damage	89	4.86		87.3±22.3		Long twisted steel	0.5	Song et al.(2015)
		89	7.48		156.0±30.2			1.0	
		89	9.99		164.2±13.4			1.5	
		89	12.5		156.5±13.4			2.0	
		92	11.8		161.4±50.7	CB		2.0	
		109	12.4		167.5±5.5	GGBS		2.0	
12	Damage	180	15.1		39.9		Long smooth steel	1.0	Kim et al.(2018)
		152	12.4		73.2		Medium smooth steel	1.0	
13	Damage		5.1		232		PVA		Ranade et al. (2014)
			4.5		66				
14	Damage				100		PVA	2.0	Hou and Lynch(2005)
					21		PVA + carbon	2.0 / 0.4	
					18		PVA + steel	2.0 / 0.1	

f'_c: compressive strength; f_t: tensile strength, GF: gauge factor.

2. Background

2.1 Fiber-Matrix Interfacial Characteristics

The fiber-matrix interfacial zone significantly influenced the fiber-matrix bond strength and, consequently, the mechanical properties of SFRCs (Abdallah et al., 2018). The fiber-matrix interfacial zone consists of (1) a thin duplex film (1 or 2 mm) in contact with the fiber, (2) outside of this, a zone with highly hydrated systems (massive calcium hydroxide crystals), and (3) outside of this, a highly porous layer parallel to the interface (Bentur et al., 1985). Ford et al.(1998) reported that the fiber-matrix interface includes an oxide passivation layer (resulting from the chemical action occurred at high pH of concrete) and/or polarization resistance/ double layers on the fiber surface. These metal oxide films enhanced the bonding between fiber and matrix (Fu and Chung, 1997) and have a high electrical resistance (Fu and Chung, 1997; Ford et al., 1998; Torrents et al., 2000; Peled et al., 2001; Suryanto et al., 2016). The fiber-matrix interface notably influenced the electrical resistance of fiber reinforced cement composites as well (Torrents et al., 2000; Peled et al., 2001; Suryanto et al., 2016).

The characteristics of a fiber-matrix interface can be evaluated

through the interfacial fiber-matrix bond strength, which is determined through single-fiber pullout (Kim et al., 2010; Le et al., 2018) or multiple-fiber pullout (Lee et al., 2010) testing using single side or double side specimens. The interfacial bond strength of the fiber-matrix is the result of physio-chemical adhesion, friction, and mechanical resistance (Naaman and Najm, 1991); however, mechanical resistance only applies to deformed fibers, such as hooked and twisted fibers. To evaluate the bond strength at the interface between the fiber and the matrix, the equivalent bond-strength per fiber (τ_{eq}) is calculated using Eq. (1), which is derived based on the curves of pullout load versus slip obtained during fiber-pullout testing (Kim et al., 2010). In this study, the bond between fiber and matrix is a shear bond strength, which resists the pullout of the fiber from the matrix (Bartos, 1981).

$$\tau_{eq} = \frac{2PE}{n_f \pi d_f L_{em}^2} \tag{1}$$

where d_f is the equivalent diameter of the fiber, L_{em} is the embedded length of the fiber, n_f is the number of embedded fibers, and PE is the pullout energy; i.e., the area under the pullout-load versus slip curve.

2.2 Electromechanical Responses of Steel Fibers Embedded in a Cement Composite Matrix During Fiber Pullout

Fig. 1 displays the electromechanical response of a typical steel-fiber-reinforced cement composite (180 MPa) during fiber
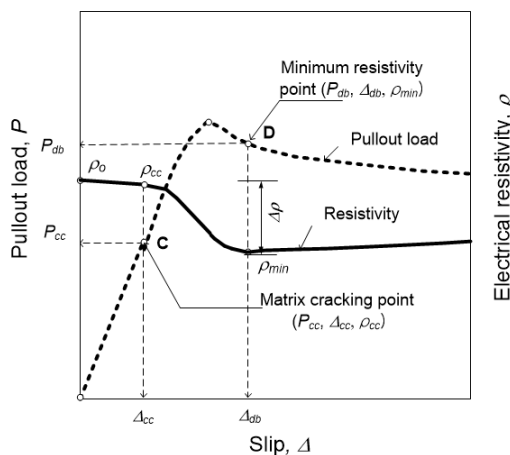
Fig. 1. The Typical Electromechanical of Multi Fiber Pullout (Le and Kim, 2017)

pullout; this response can be divided into three stages, namely linear elastic bonding, fiber debonding, and fiber slip stages (Le and Kim, 2017). The linear elastic bonding stage occurs between points 0 and C (the matrix cracking point) as slip increased from 0 to ρ_{cc}. After matrix cracking, as slip increased from ρ_{cc} to ρ_{db} during the fiber-debonding stage, fiber debonding commences at point C, with full fiber debonding occurring at point D. Finally, fiber slip starts at point D and continues to the end point. The matrix cracking point (C) and the full debonding point (D) are determined in the pullout load–electrical resistivity versus slip curves (Le and Kim, 2017).

During the linear elastic bonding stage and prior to matrix cracking, the electrical resistivity changes very little with increasing applied pullout load, since the fiber and matrix are fully bonded. Subsequently, during the fiber-debonding stage following matrix cracking, the electrical resistivity decreases remarkably from that at the matrix-cracking point (ρ_{cc}) to the minimum electrical resistivity at the full fiber-debonding point (ρ_{min}), as a result of debonding at the interface. Finally, the electrical resistivity increases during the fiber-slip stage, owing to increased voids (phases of high electrical resistivity) between the fiber and the matrix with increasing fiber slip. Fiber pullout resistance in this stage is governed by the friction at the interface between the fiber and the matrix.

The reduction in electrical resistivity during the fiber-debonding stage was reported to be the source of HPFRCC self-damage capacity (Le and Kim, 2017). The electrical resistivity response during the fiber-debonding stage was notably dependent on the bond strength between the fiber and the matrix at the interface. Hence, the characteristics of the interfacial fiber-matrix bond and their effects on the electrical resistivity of steel-fiber-reinforced cement composites during fiber de-bonding still require careful investigation.

3. Experimental Method

Fig. 2 shows the experimental program used to investigate the effects of interfacial fiber-matrix characteristics with different matrix strengths, fiber geometries, and coating materials on the electrical resistivity of steel-fiber-reinforced cement composites. Multifiber pullout specimens (one-cold-joint specimens) were designed according to Le and Kim (2017), as can be seen in Fig. 3.
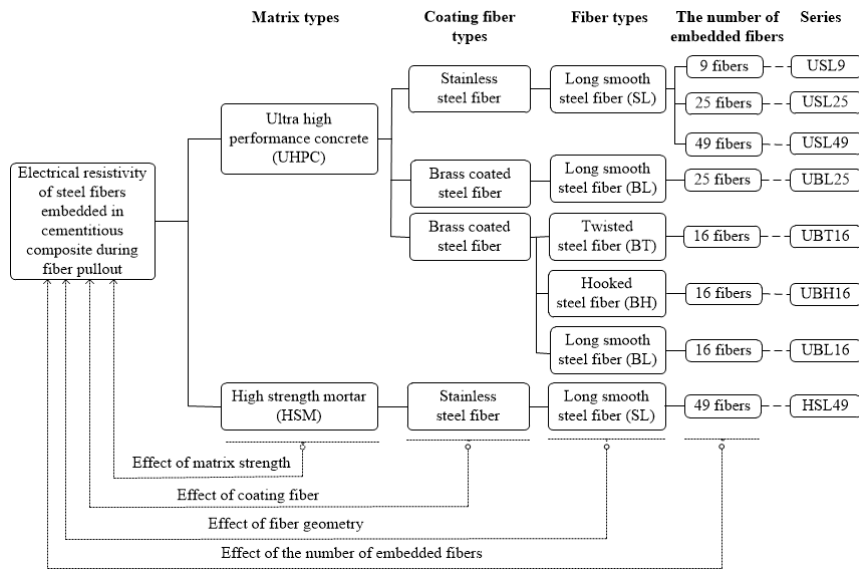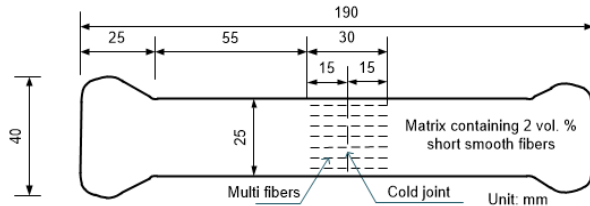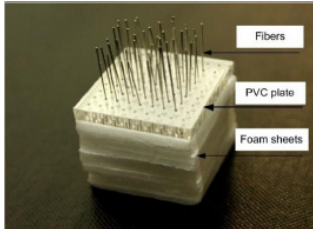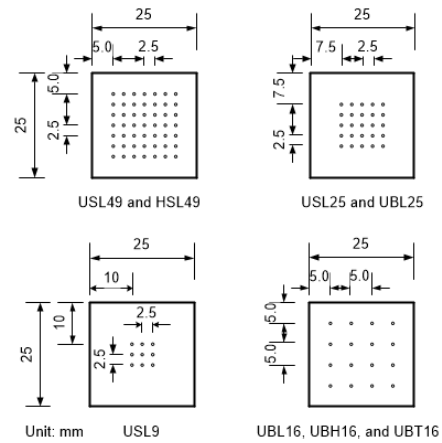
Fig. 2. Experimental Program

(a) Multi-Fiber Pullout Specimen

(b) Align Multi-Fibers Using PVC Plate and Foam Sheets (Le and Kim, 2017)

(c) Fiber Distribution at Cold Joint Section

(d) USL49 After Tests (Smooth Fibers)

(e) UBH16 After Tests (Hooked Fibers)

(f) UBT16 After Tests (All Twisted Fibers Broke)

Fig. 3. Geometry of Multi-Fiber Pullout Specimens

Each specimen (Fig. 3(a)) was 190 mm long and had a cross section of 25 mm × 25 mm. Two parts of specimens were connected by bonding of matrices and embedded fibers at the cold joint position. Under tension, the matrix at the cold joint position was firstly cracked and the embedded fibers were then debonded and pulled out. Ultra-high-performance concrete (UHPC) and high strength mortar (HSM) containing 2.0 vol % short smooth steel fibers (6 mm in length) were used as the matrices of the multifiber-pullout

Table 2. Composition of Matrix by Weight Ratio, Compressive Strength, and Electrical Resistivity

Notation	Cement (Type)	Silica fume	Silica powder	Silica sand	Fly ash	Water	Super plasticizer (Type)	Smooth steel fiber vol %	Compressive strength (MPa)	ρ_M (kΩ-cm)
UHPC	1 (I)	0.25	0.3	1.1	-	0.2	0.067 (A)	2.0	180	1560
HSM	1 (III)	-	-	1.0	0.15	0.35	0.0055 (B)	2.0	95	300

Type A contained 30 % solid content. Type B contained 25 % solid content. ρ_M: the electrical resistivity of the matrices.

Table 3. Properties of High Strength Steel Fibers

Notation	Fiber type	Coating type	Diameter (mm)	Length (mm)	Tensile strength (MPa)	Elastic modulus (GPa)	Electrical resistivity (10^{-8} kΩ-cm)
SL	Long smooth fiber	Stainless	0.3	30	2428	200	8.48
SS	Short smooth fiber	Stainless	0.2	6	2104	200	8.48
BL	Long smooth fiber	Brass	0.3	30	2580	200	2.10
BH	Hooked fiber	Brass	0.375	30	2311	200	1.95
BT	Twisted fiber	Brass	0.3	30	2104	200	2.21

specimens. The compressive strengths of the UHPC and HSM were 180 and 95 MPa, respectively. As summarized in Table 2, the electrical resistivity of UHPC matrix (1560 $k\Omega$-cm) is significantly higher than that of HSM matrix (300 $k\Omega$-cm) owing to high density of the UHPC matrix. In actual condition, fibers are not aligned, the random fiber orientation would be influence the electrical resistivity response of the composite after matrix cracking owing to the connection of fibers at crack position. The effect of fiber orientation on the electrical resistivity response should be further investigated.

Short smooth steel fibers were distributed to prevent matrix cracking, except for the pre-designated crack (cold joint) position. At the pre-designated crack position, 30-mm-long steel fibers with different surface coating (stainless and brass-coated fibers) and different geometries (straight, hooked, and twisted fibers) were embedded in the middle of the specimens to depths of 15 mm, as can be seen in Fig. 3(a). Adopted from Le and Kim (2017), 49 fibers, which were equivalent to approximately 1.0 vol % in a 2D distribution, were embedded in the matrices of USL49 and HSL49. As the deformed fibers and brass coated fibers produced higher fiber-matrix bond strength than the straight fibers and stainless steel fibers, respectively, 16 and 25 fibers were embedded in the matrices of UBT16, UBH16, UBL16, USL25, and UBL25 in order to provide only a crack at the cold joint position.

3.1 Material and Specimen Preparation

Table 2 lists the ratios (by weight) of the matrix components of the UHPC and HSM, while Table 3 summarizes the properties of the steel fibers used in these experiments. The matrix composition and strength of the UHPC matrix was adopted from Kim et al. (2018) while those of the HSM matrix was adopted from Kim and Kim (2018). Cement Type I (according to ASTM standard) and superplasticizer Type A with 30 % solid content were used for the UHPC while cement Type III and superplasticizer Type B with 25 % solid content were used for the HSM. The silica sand had an average diameter of 0.2 mm. The average diameters of silica powder and silica fume are 10 mm and 0.1 mm, respectively. The silica powder and silica fume contain more than 98 % SiO_2.

Multifiber pullout specimens were prepared following the procedure described by Le and Kim (2017), which includes two different mixing and casting processes. Foam sheets and PVA plates with designed holes were used to align fibers (Fig. 3(b)) and fix embedded length of multi-fiber at the cold joint position (Le and Kim, 2017). The PVA plate was removed prior to embedding foam sheets with fibers into molds. Half of the specimen was first mixed, cast, and cured in a water tank at suitable temperature to reach the strength. The foam sheets were removed and the other half of the specimen was then manufactured. Two parts of specimens were connected at the cold joint by bonding of matrices and embedded fibers. Figs. 3(d), 3(e), and 3(f) show images of specimens after multi-fiber pullout.

A 20-L Hobart-type laboratory mixer was used to prepare the fiber pullout specimens. All of the components of the UHPC matrix (including the silica fume, cement, silica powder, and silica sand) or the HSM matrix (including the cement, fly ash, and silica sand) were first dry-mixed for 5 min. Water was then added followed by mixing for a further 5 min. Super-plasticizers were gradually added, with further mixing for approximately 5 min. As the mixtures showed suitable workabilities and viscosities for

uniform fiber distribution (mini slump flow was around 220–230 mm), short smooth fibers were carefully dispersed by hand into the mixtures, after which they were mixed for a further 1 min. The short-fiber-containing matrix mixtures were poured into molds with gentle vibration to minimize interior air bubbles. All specimens were then covered with plastic sheets and stored at room temperature (20 ± 2°C) for 48 h, after which they were demolded. The UHPC-matrix specimens were cured in a water tank at 90°C for 3 d, while the HSM-matrix specimens were cured in a water tank at 20°C for 14 d. The surface of each specimen was carefully ground prior to coating with silver paint and copper tape at the electrode positions.

3.2 Test Setup

Fig. 4 displays the experimental set-up for determining electrical resistance during multifiber pullout testing. The fiber-pullout experiments were performed using a universal testing machine (SHMC 1012) manufactured in Korea, while electrical resistance was measured using a Fluke 8846A multimeter with the four-probe method. The machine-displacement speed was maintained at 1.0 mm/min during testing. The pullout load was measured using a load cell with 4905 N (500 kgf) capacity, while slip was measured using a linear variable differential transformer (LVDT) attached to the upper grip. A 10-mA direct current (DC) was applied through two outer electrodes, while the voltage between the two inner electrodes was measured in order to determine the electrical resistance. The electrodes were fabricated on the surfaces
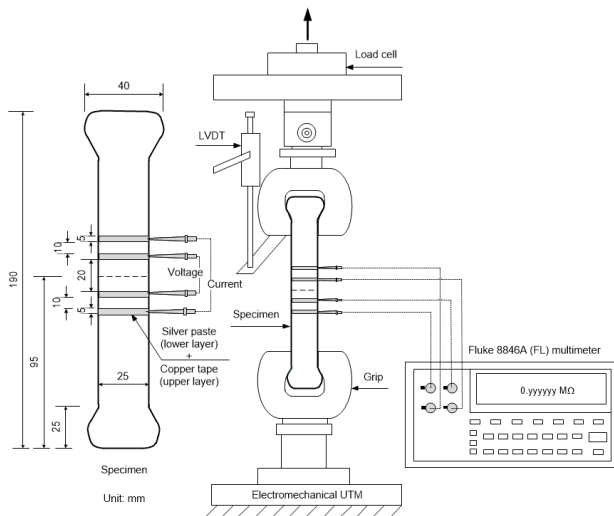
of the specimens using copper tape and silver paint. The electrical resistivity (ρ) of each specimen was calculated using Eq. (2):

$$\rho = R\frac{A}{L} \qquad (2)$$

where R is the electrical resistance, A is the cross-sectional area, and L is the gauge length between the two inner electrodes. Prior to loading, specimens were stabilized for at least 30 min to minimize the effects of electrical polarization. The initial resistivity of each specimen (ρ_o) was determined at the end of the polarization time. Three identical specimens were subjected to testing in each case.

4. Results

4.1 Effect of Matrix Strength on the Electromechanical Response

The UHPC specimens, with higher matrix strengths, clearly exhibited higher interfacial bond strength as well as higher reductions in electrical resistivity during fiber pullout than the HSM specimens. Furthermore, during the linear elastic bonding

Fig. 4. Test Set-Up for Measuring the Electrical Resistivity During Multi-Fiber Pullout
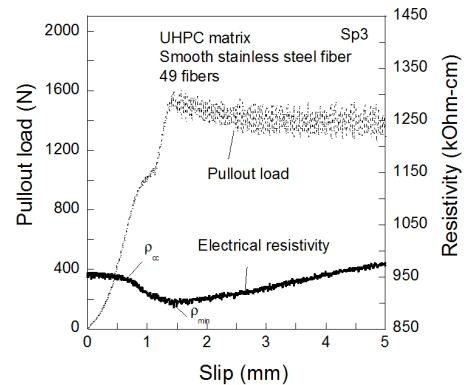
(a) USL49 Specimen with UHPC Matrix
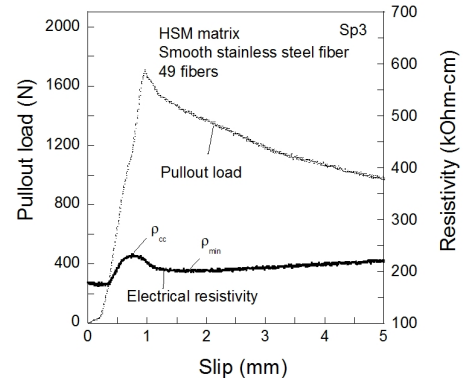
(b) HSL49 Specimen with HSM Matrix

Fig. 5. Effect of Matrix Strength on the Electromechanical Response

Table 4. The Electro-Mechanical Characteristics

Notation	PE N·mm	τ_{eq} MPa	Δ_{cc} mm	Δ_{db} mm	$\Delta_{db} - \Delta_{cc}$ mm	ρ_o kΩ-cm	ρ_{cc} kΩ-cm	$\rho_{\min}$ kΩ-cm	$\Delta\rho = \rho_{cc} - \rho_{\min}$ kΩ-cm
USL49 (49 stainless steel fibers embedded in UHPC matrix)									
Sp1	14337.3	2.8	0.7	2.0	1.3	874.5	865.1	803.2	61.9
Sp2	15231.7	2.9	0.5	3.1	2.6	842.2	833.9	786.8	47.0
Sp3	16933.6	3.3	0.8	1.5	0.7	949.8	943.7	892.1	51.6
Average	15500.9	3.0	0.7	2.2	1.5	888.8	880.9	827.4	53.5
HSL49 (49 stainless steel fibers embedded in HSM matrix)									
Sp1	11646.7	2.2	0.7	1.7	1.0	179.0	230.3	198.2	32.0
Sp2	10027.1	1.9	0.8	1.6	0.9	280.4	339.8	310.4	29.4
Sp3	11545.7	2.2	0.7	1.4	0.6	239.9	300.3	265.1	35.1
Average	11073.2	2.1	0.7	1.6	0.8	233.1	290.1	257.9	32.2
UBL25 (25 brass coated steel fibers embedded in UHPC matrix)									
Sp1	13427.9	5.1	0.5	1.3	0.8	1153.7	1160.4	1132.8	27.6
Sp2	14574.4	5.5	0.4	1.9	1.5	1111.5	1112.9	1055.3	57.6
Sp3	16558.1	6.2	0.7	1.9	1.1	1159.5	1164.3	1088.4	75.9
Average	14853.5	5.6	0.6	1.7	1.1	1141.6	1145.9	1092.2	53.7
USL25 (25 stainless steel fibers embedded in UHPC matrix)									
Sp1	7224.6	2.7	0.5	1.0	0.5	1210.3	1222.4	1173.5	36.8
Sp2	7965.7	3.0	0.5	1.0	0.5	1262.4	1262.7	1211.4	51.0
Sp3	7061.1	2.7	0.7	1.5	0.8	1076.7	1080.7	1048.4	28.3
Average	7417.1	2.8	0.6	1.2	0.6	1183.1	1188.6	1144.4	38.7
UBL16 (16 brass coated smooth fibers embedded in UHPC matrix)									
Sp1	9561.7	5.6	0.3	0.6	0.2	1028.8	1030.5	1019.8	10.7
Sp2	7937.5	4.7	0.4	0.8	0.4	1017.9	1020.7	997.1	23.6
Sp3	7406.9	4.4	0.3	1.0	0.7	1124.0	1120.5	1110.5	10.0
Average	8302.0	4.9	0.3	1.0	0.4	1056.9	1057.2	1042.5	14.8
UBH16 (16 brass coated hooked fibers embedded in UHPC matrix)									
Sp1	11646.7	5.5	0.7	1.7	1.0	1137.1	1138.8	1067.7	71.2
Sp2	10027.1	4.7	0.8	2.0	1.2	1067.0	1071.8	1029.3	42.5
Sp3	11545.7	5.4	0.7	1.9	1.2	779.1	772.6	730.8	41.8
Average	11073.2	5.2	0.7	1.6	1.1	994.4	994.4	942.6	51.8
UBT16 (16 brass coated twisted fibers embedded in UHPC matrix)									
Sp1	2737.1	1.6	0.8	0.8	0.0	1322.4	1322.4	1315.5	6.9
Sp2	2762.7	1.6	0.7	0.8	0.1	1397.1	1381.4	1378.0	3.4
Sp3	3402.3	2.0	0.9	0.9	0.0	1178.3	1175.9	1174.0	1.9
Average	2967.3	1.7	0.8	0.9	0.1	1299.3	1293.3	1289.2	4.1
USL9 (9 stainless steel fibers embedded in UHPC matrix)									
Sp1	2207.1	2.3	0.1	0.4	0.3	1315.1	1316.5	1309.2	7.4
Sp2	1886.9	2.0	0.1	0.6	0.4	1277.0	1277.0	1250.2	26.8
Sp3	2527.4	2.6	0.1	0.5	0.3	1315.5	1318.9	1305.2	13.7
Average	2207.1	2.3	0.1	0.5	0.4	1302.5	1304.1	1288.2	16.0

stage, the electrical resistivities of the UHPC-matrix specimens changed little, whereas those with the HSM matrix increased.

Fig. 5 displays changes in both pullout load and electrical resistivity with increasing multifiber slip. The pullout resistance of the USL49 specimen (UHPC matrix) was higher than that of the HSL49 specimen (HSM matrix). As shown in Fig. 5, the pullout energy (the area under the pullout load versus slip curve) of USL49 was much higher than that of HSL49. The equivalent bond strengths of the USL49 and HSL49 specimens were determined to be 3.0 and

2.1 MPa, respectively. The amounts of slip at their cracking points (Δ_{cc}) and the full-debonding points (Δ_{db}) were determined according to (Le and Kim, 2017) and are summarized in Table 4.

It was interesting to observe that the electrical resistivity of the USL49 specimen with UHPC matrix changed little during the linear elastic bonding stage, whereas that of the HSL49 specimen with HSM matrix increased. After matrix cracking, the USL49 specimen exhibited a higher reduction in electrical resistivity ($\Delta\rho = \rho_{cc} - \rho_{min}$) than the HSL49 specimen; these reductions for USL49

and HSL49 were 53.5 and 32.2 $k\Omega$-cm, respectively. During the fiber-slip stage, the electrical resistivities of both the USL49 and HSL49 specimens gradually increased. Furthermore, the initial electrical resistivity of HSL49 (233.1 $k\Omega$-cm) was significantly lower than that of the USL49 specimen (888.8 $k\Omega$-cm).

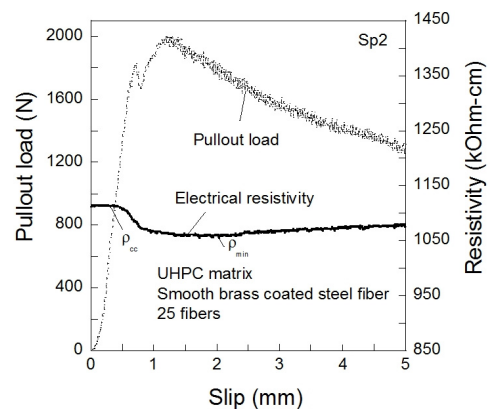## 4.2 Effect of the Fiber Coating on the Electromechanical Response

Brass coated steel fibers produced both remarkably higher interfacial bond strength and a greater reduction in the electrical resistivity during the fiber-debonding stage than stainless steel fibers.

Fig. 6 shows the pullout loads (and/or electrical resistivities) as functions of slip for specimens containing stainless steel fibers (USL25) and brass-coated steel fibers (UBL25). The pullout resistance of the UBL25 specimen was clearly higher than that of the USL25 specimen. As shown in Fig. 6, the area under the pullout load versus slip curve of the UBL25 specimen was remarkably higher than that of the USL25 specimen. As summarized in Table 4, the average value of the equivalent bond strengths of the UBL25 (5.6 MPa) was notably higher than that of USL25 specimens (2.8 MPa).

The electrical resistivity responses of both the USL25 and UBL25 specimens with UHPC matrices exhibited the three typical stages shown in Fig. 1. The reduction in the electrical resistivity of UBL25 was remarkably higher than that of USL25. Table 4 reveals that the reductions in the electrical resistivities of the UBL25 and USL25 specimens were 53.7 and 38.7 $k\Omega$-cm, respectively. The initial electrical resistivity of UBL25 (1145.9 $k\Omega$-cm) was slightly lower than that of USL25 (1188.6 $k\Omega$-cm).
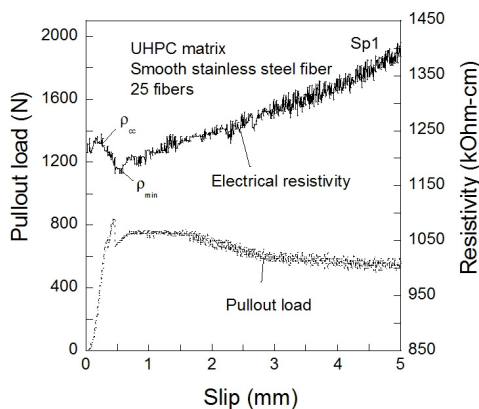
4.3 Effect of the Fiber Geometry on Electromechanical Response

Hooked steel fibers resulted in higher interfacial bond strengths as well as higher reductions in electrical resistivity than straight steel fibers, while the specimen containing twisted fibers did not exhibit any reduction in electrical resistivity as all of the fibers broke immediately after matrix cracking, a consequence of a very high interfacial bond strength (Park et al., 2014).

Fig. 7 displays the electromechanical pullout responses of specimens containing smooth fibers (UBL16), hooked fibers (UBH16), and twisted fibers (UBT16). The UBH16 specimen (with hooked fibers) exhibited higher interfacial bond strength than the UBL16 specimen (with smooth fibers). As shown in Figs. 7(a) and 7(b), the pullout energy of UBH16 was clearly higher than that of UBL16. All twisted fibers broke immediately following matrix cracking as the pullout stress exceeded the fiber-failure strength, as can be seen in Fig. 7(c) and Fig. 3(f). As summarized in Table 4, the equivalent bond strengths of UBL16 and UBH16 were 4.9 and 5.2 MPa, respectively while that of UBT16 was 1.7 MPa.

During fiber pullout, the specimens with hooked and smooth fibers also showed three stages of electrical resistivity, similar to the typical response shown in Fig. 1. However, the electrical resistivity of the specimen with the twisted fibers changed little during the elastic stage, and then increased significantly, which is ascribed to fiber breakage immediately after matrix cracking. The reduction in the electrical resistivity of the UBH16 specimen (hooked fibers, 51.8 $k\Omega$-cm) was notably higher than that of UBL16 (smooth fibers, 12.4 $k\Omega$-cm).

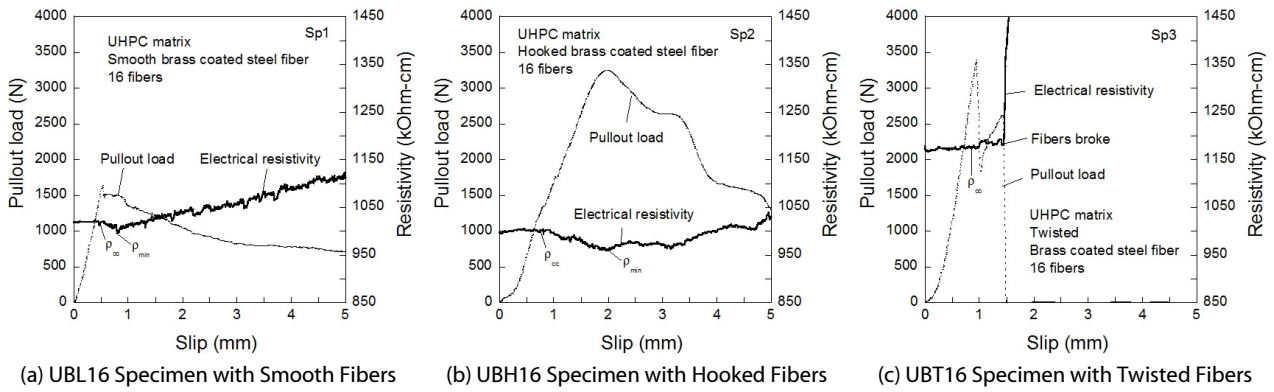As the number of embedded fibers at the cold joints increased,

(a) USL25 Specimen with Stainless Steel Fibers

(b) UBL25 Specimen with Brass Coated Steel Fibers

Fig. 6. Effect of Coating Material of Fibers on the Electromechanical Response

(a) UBL16 Specimen with Smooth Fibers   (b) UBH16 Specimen with Hooked Fibers   (c) UBT16 Specimen with Twisted Fibers

Fig. 7. Effect of Fiber Geometry on the Electromechanical Response

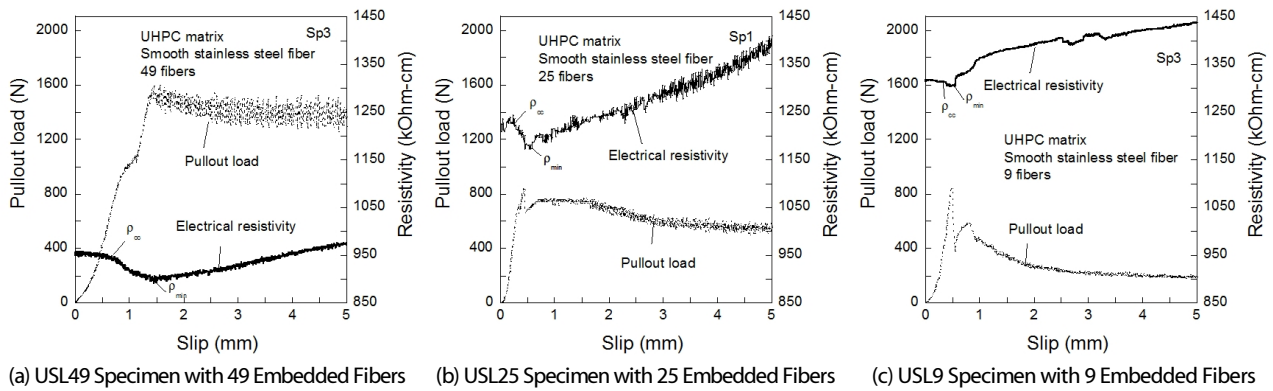(a) USL49 Specimen with 49 Embedded Fibers   (b) USL25 Specimen with 25 Embedded Fibers   (c) USL9 Specimen with 9 Embedded Fibers

Fig. 8. Effect of Different the Number of Embedded Fibers on the Electromechanical Response

the reductions in the electrical resistivities of the composites also increased. Fig. 8 shows the electro-mechanical pullout responses of specimens with nine, 25, and 49 embedded fibers, namely USL9, USL25, and USL49, respectively. Fig. 8 reveals that the pullout response depends on the number of embedded fibers. It is clear that the area under the pullout load versus slip curve increases with increasing numbers of embedded fibers. As summarized in Table 4, the values of the equivalent bond strength per fiber-matrix were 2.3, 2.8, and 3.0 MPa for the USL9, USL25, and USL49 specimens, respectively. The interfacial bond strength, based on the pullout energies, increased with increasing numbers of fibers.

4.4 Effect of the Number of Embedded Fibers on the Electromechanical Response

The electrical-resistivity responses of the USL9, USL25, and USL49 specimens also exhibited the three typical stages during fiber pullout (Fig. 1). During fiber debonding, the reduction in electrical resistivity increased as the number of embedded fibers increased. As shown in Table 4, the reductions in electrical

resistivity of the USL9, USL25, and USL49 specimens were 16.0, 38.7, and 53.5 $k\Omega$-cm, respectively. The electrical resistivity clearly decreases with increasing numbers of embedded fibers. As listed in Table 4, the initial electrical resistivities (ρ_o) of USL9, USL25, and USL49 were 1302.5, 1183.1, and 888.8 $k\Omega$-cm, respectively

5. Discussion

5.1 Correlation between the Interfacial Bond Strength and the Reduction in Electrical Resistivity

Fig. 9 displays the correlation between interfacial bond characteristics (the interfacial bond strength) and the reductions in the electrical resistivities of specimens with different matrices (Fig. 9(a)), fiber coatings (Fig. 9(b)), fiber geometries (Fig. 9(c)), and numbers of embedded fibers (Fig. 9(d)). A higher interfacial bond strength generally produced higher reduction in electrical resistivity during fiber debonding, after matrix cracking. It can be primarily due to the reduction in electrical resistivity at the
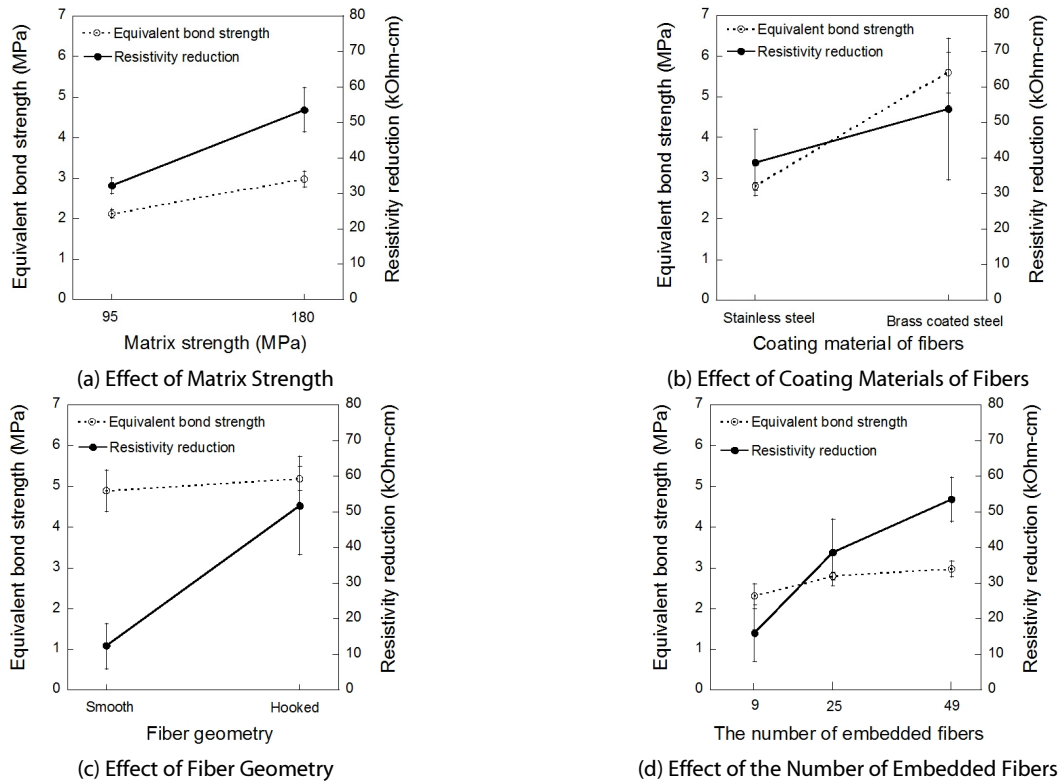
Fig. 9. Effect of Interfacial Bond Characteristics on the Electrical Resistivity Reduction

(a) Effect of Matrix Strength

(b) Effect of Coating Materials of Fibers

(c) Effect of Fiber Geometry

(d) Effect of the Number of Embedded Fibers

fiber-matrix interface. The reduction in electrical resistivity increased with more fiber-matrix debonded part, as shown in Figs. 5~8. The electrical resistivity of the fiber-matrix interface includes the electrical resistivity of the interfacial transition zone (ITZ) of the surrounding matrix fiber and the high electrical resistivity of metal oxides and/or other components on the surface of fibers (Fu and Chung, 1997). Under pullout load, at debonded part, the high electrical resistivity phase on the surface of fibers (metal oxides and/or other components) decreases and consequently results in the reduction in electrical resistivity during fiber-matrix debonding. As can be seen in Fig. 10, the metal oxide or other components (high electrical resistivity) on the fiber surface significantly decreased after fiber pullout. Thus, a higher bond strength (higher pullout load) causes a greater reduction in high electrical resistivity phase (oxide passivation layer and/or other components) of the fiber-matrix interface during fiber-matrix debonding and results in greater reduction in electrical resistivity of the composite during fiber matrix debonding. In case of using coarse aggregates, the effect of coarse aggregate on electrical resistivity response should be further investigated.

As shown in Fig. 9(a), the reduction in electrical resistivity during fiber debonding increases with increasing matrix strength. A stronger matrix (including UHPC) generally exhibits denser ITZ microstructures; consequently the interfacial bond strength increases (Kim et al., 2010). Under pullout load, higher matrix strength can produce a greater reduction of the high electrical resistivity phase (metal oxides film and/or other components) on the fiber surface. Hence, during fiber debonding, the reduction in the electrical resistivity of USL49 (with the higher matrix strength) was higher than that of the HSL49 specimen owing to a greater reduction of the high electrical resistivity phase (metal oxides film and/or other components) on the surface of the fibers and the higher electrical resistivity of the fiber-matrix interface.

As shown in Fig. 9(b), the specimen with brass-coated-steel-fibers produced a higher reduction in electrical resistivity during fiber pullout than the specimen containing stainless-steel fibers because the interfacial bond strength of the former was higher, as shown in Fig. 6. Al Khalaf et al.(1980) also reported that the bond strengths at the interfaces between brass-coated steel fibers and the matrix were higher than those involving stainless steel
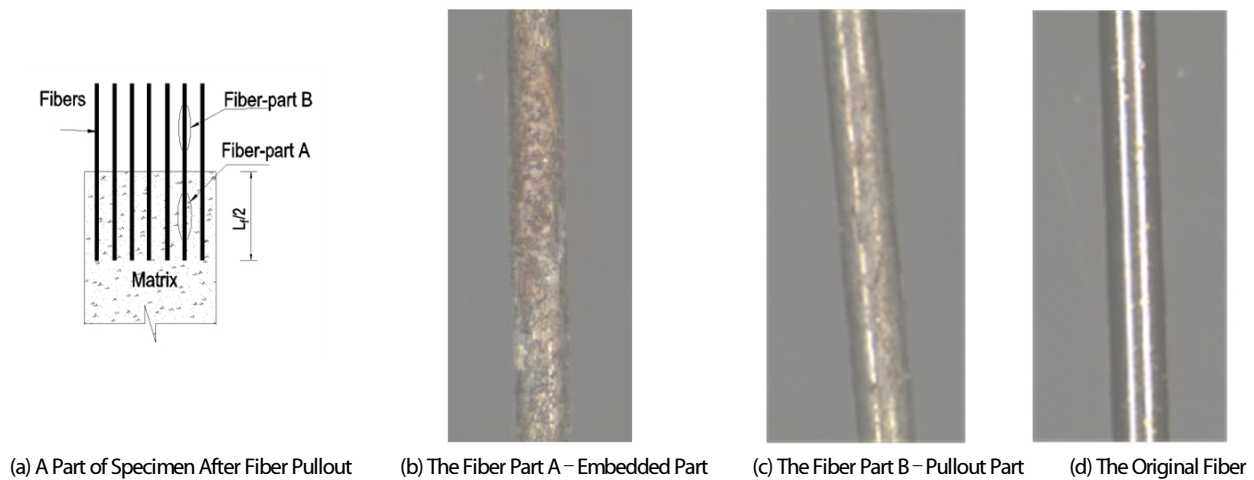
(a) A Part of Specimen After Fiber Pullout   (b) The Fiber Part A – Embedded Part   (c) The Fiber Part B – Pullout Part   (d) The Original Fiber

Fig. 10. The Microscope Images of Fiber Embedded in Matrix and After Fiber Pullout

fibers owing to the greater adhesiveness between the brass-coated fibers and the matrix. Brass becomes involved in chemical reactions while in contact with the mortar matrix (Al Khalaf and Page, 1979), which results in a stronger adhesive bond between the fiber and the matrix. These chemical reactions may produce metal oxides at the fiber-matrix interface, which are phases with high electrical resistivities (Fu and Chung, 1997). In addition, the brass-coated material exhibited higher fiber conductivity or lower electrical resistivity. Hence, during fiber debonding, higher bond strength (pullout resistance) of brass-coated fibers causes greater reduction in the high electrical resistivity phase at fiber-matrix interface and consequently greater reduction in electrical resistivity of the composite.

Fig. 9(c) reveals the relationships between fiber geometry (smooth and hooked) and the interfacial bond strength, as well as the reduction in electrical resistivity of the composite during fiber debonding. Hooked fibers result in a higher interfacial bond strength and a higher reduction in electrical resistivity than smooth fibers. The higher interfacial bond strengths between the hooked fibers and the matrix are ascribed to mechanical resistance (Naaman and Najm, 1991; Wu et al., 2018). Moreover, the geometries of the hooked fibers result in a higher fiber-debonding length during fiber pullout, which causes a higher reduction in electrical resistivity. Furthermore, the higher bond of the hooked fibers owing to mechanical bonding can produce a greater reduction of the high electrical resistivity phase (metal oxide film and/or other components) on the surface of the fibers during fiber debonding. Hence, during fiber debonding, the reductions in the

electrical resistivities of the specimens containing the hooked steel fibers were higher than those of the specimens with the smooth-steel fibers, owing to a greater reduction of the high electrical resistivity phase at the fiber-matrix interface and higher debonding length during fiber debonding. The reduction in the electrical resistivity of the specimens with twisted steel fibers cannot be observed because the length of the fiber-matrix interfacial debonding is zero owing to the breakage of all fibers immediately after the matrix cracking.

As shown in Fig. 9(d), the equivalent bond strength increases with increasing numbers of embedded fibers, as does the reduction in electrical resistivity during fiber debonding. As is evident in Fig. 8, the pullout loads of the USL9 specimen (nine fibers) exhibited softening behavior, since the pullout load dropped following matrix cracking. In contrast, the pullout loads of the USL25 and USL49 specimens (25 and 49 fibers, respectively) showed slip-hardening behavior, in which the pullout load continued to increase after matrix cracking; hence, the pullout energy and the equivalent bond strength both increased as a consequence. In addition, as the number of embedded steel fibers increased, the amount of interfacial fiber-matrix debonding in the composite increases. Consequently, the reduction in electrical resistivity increases during fiber debonding.

5.2 Correlation between Matrix Strength and Electrical-Resistivity Response in the Elastic Region

The electrical resistivity of USL49 (UHPC matrix) changed little in the elastic region, whereas that of HSL49 (HSM matrix)

(a) Specimens with UHPC Matrix   (b) Specimens with HSM Matrix

Fig. 11. Conductive Network of Specimens with UHPC and HSM Matrices

increased, which is possibly due to the different electrical-resistivity responses of matrices with different conductive networks under tension. The flow of electrical current in steel-fiber-reinforced concrete involves a conductive fiber network and mobile ions in the pore-solution system of the matrix (Hou and Lynch, 2005). The conductive network of both the USL49 and the HSL49 in the gauge length included the connection of 2.0 vol % short smooth fibers, 49 embedded fibers, and porous solution system in their matrices. The HSM matrix has higher water per cement ratio and consequently facilitates a high number of connections between adjacent conductive fibers and the pore-solution system, as shown in Fig. 11. On the other hand, the microstructure of the UHPC matrix contains very small discontinuous pores (Wang et al., 2015), and hence the conductivity of the USL49 specimen is primarily influenced by the conductive steel-fiber network rather than connections involving the pore-solution system. Under tensile load, the electrical conductivities of the specimens containing the HSM matrix significantly decrease owing to disconnections between the pore-solution system and the fiber network, whereas the conductivities of the specimens containing the UHPC matrix are largely unaffected. Consequently, in the elastic region, as the pullout load increases, the electrical resistivity of the HSM matrix increases, while that of the UHPC matrix changes little. Wen and Chung (2003) also observed an increase in the electrical resistivity of 0.72 vol % steel-fiber-reinforced concrete (high pore system) in the elastic region owing to changes in the conductive network under tension.

6. Conclusions

This experimental study investigated the effects of matrix strength, fiber type, and fiber content on the electrical resistivity of the steel-fiber-reinforced cement composite during fiber pullout.

We carefully determined the effects of different interfacial bond characteristics on electrical resistivity by investigating different matrix strengths, fiber geometries, fiber coatings, and numbers of embedded fibers. The following conclusions are drawn.

(1) A higher interfacial bond strength results in a higher reduction in electrical resistance during fiber debonding due to the higher electrical resistivity at the fiber-matrix interface, a greater reduction of the high electrical resistivity phase (metal oxides and/or other components) on the surface of fibers during fiber debonding, and higher debonding length of the fiber-matrix.

(2) Brass-coated steel fibers result in much higher equivalent bond strengths as well as greater reductions in electrical resistivity than stainless-steel fibers.

(3) The higher interfacial bond strength of the specimens with hooked fibers result in higher reductions in electrical resistivity compared to specimens with smooth fibers.

(4) The reduction in the electrical resistivity of the specimens with twisted steel fibers embedded in UHPC matrix cannot be observed because the length of the fiber-matrix interfacial debonding is zero owing to the breakage of all fibers immediately after the matrix cracking.

(5) Greater numbers of conductive steel fibers that bridge cracks facilitate higher reductions in electrical resistivity.

(6) The self-damage-sensing ability of an HPFRCC under tension clearly depends on the characteristics of the interfacial fiber-matrix bond, the matrix, and the fibers that bridge cracks.

(7) The HSM matrix (95 MPa) produced a better electrical resistivity response than the UHPC matrix (180 MPa) in the elastic region due to a stronger connection between the pore solution system and conductive network of fibers.

Acknowledgements

References

Abdallah, S., Fan, M. and Rees, D. W. A. (2018). "bonding mechanisms and strength of steel fiber-reinforced cementitious composites: Overview." *Journal of Materials in Civil Engineering*, Vol. 30, No. 3, p. 04018001. doi: 10.1061/(ASCE)MT.1943-5533.0002154.

Al Khalaf, M. N. and Page, C. L. (1979). "Steel/mortar interfaces: Microstructural features and mode of failure." *Cement and Concrete Research*, Vol. 9, No. 2, pp. 197-207. doi: 10.1016/0008-8846(79)90026-7.

Al Khalaf, M. N., Page, C. L. and Ritchie, A. G. B. (1980). "Effects of fibre surface composition on mechanical properties of steel fibre reinforced mortars." *Cement and Concrete Research*, Vol. 10, No. 1, pp. 71-77.

Alwan, J. M., Naaman, A. and Hansen, W. (1991). "Pull-out work of steel fibers from cementitious composites?: Analytical investigation." *Cement & Concrete Composites*, Vol. 13, No. 4, pp. 247-255. doi: 10.1016/0958-9465(91)90030-L.

Azhari, F. and Banthia, N. (2012). "Cement-based sensors with carbon fibers and carbon nanotubes for piezoresistive sensing." *Cement and Concrete Composites*, Vol. 34, No. 7, pp. 866-873. doi: 10.1016/j.cemconcomp.2012.04.007.

Bartos, P. (1981). "Review paper: Bond in fibre reinforced cements and concretes." *The International Journal of Cement Composites*, Vol. 3, No. 3, pp. 159-177.

Bentur, A. and Alexander, M. G. (2000). "A review of the work of the RILEM TC 159-ETC: Engineering of the interfacial transition zone in cementitious composites." *Materials and Structures*, Vol. 33, No. 2, pp. 82-87. doi: 10.1007/BF02484160.

Bentur, A., Diamond, S. and Mindess, S. (1985). "The microstructure of the steel fibre-cement interface." *Journal of Materials Science*, Vol. 20, No. 10, pp. 3610-3620. doi: 10.1007/BF01113768.

Bontea, D. M., Chung, D. D. L. and Lee, G. C. (2000). "Damage in carbon fiber-reinforced concrete, monitored by electrical resistance measurement." *Cement and Concrete Research*, Vol. 30, No. 4, pp. 651-659. doi: 10.1016/S0008-8846(00)00204-0.

Chan, Y. W. and Chu, S. H. (2004). "Effect of silica fume on steel fiber bond characteristics in reactive powder concrete." *Cement and Concrete Research*, Vol. 34, No. 7, pp. 1167-1172. doi: 10.1016/j.cemconres.2003.12.023.

Chung, D. D. L. (2002). "Piezoresistive cement-based materials for strain sensing." *Journal of Intelligent Material Systems and Structures*,

Vol. 13, No. 9, pp. 599-609. doi: 10.1106/104538902031861.

Ford, S. J., Shane, J. D. and Mason, T. O. (1998). "Assigment of features in impedance spectra of the cement paste/steel system." *Cement and Concrete Research*, Vol. 28, No. 12, pp. 1737-1751.

Fu, X and Chung, D. D. L. (1997). "Bond strength and contact electrical resistivity between cement and stainless steel fiber: their correlation and dependence on fiber surface treatment and curing age." *ACI Materials Journal*, Vol. 94, No. 3, pp. 203-208.

Fu, X., Lu, W. and Chung, D. D. L. (1998). "Improving the Strain-sensing ability of carbon fiber-reinforced cement by ozone treatment of the fibers." *Cement and Concrete Research*, Vol. 28, No. 2, pp. 183-187. doi: 10.1016/S0008-8846(97)00265-2.

Han, B. and Ou, J. (2007). "Embedded piezoresistive cement-based stress/strain sensor." *Sensors and Actuators, A: Physical*, Vol. 138, No. 2, pp. 294-298. doi: 10.1016/j.sna.2007.05.011.

Han, B., Yu, X. and Kwon, E. (2009). "A self-sensing carbon nanotube/ cement composite for traffic monitoring." *Nanotechnology*, Vol. 20, No. 44, pp. 1-5. doi: 10.1088/0957-4484/20/44/445501.

Han, B., Yu, X. and Ou, J. (2014). *Self-sensing concrete in smart structures*, Butterworth Heinemann, Kindlington.

Han, B., Zhang K., Yu, X., Kwon, E. and Ou, J. (2011). "Nickel particle-based self-sensing pavement for vehicle detection." *Measurement: Journal of the International Measurement Confederation*, Vol. 44, No. 9, pp. 1645-1650. doi: 10.1016/j.measurement.2011.06.014.

Han, B., Zhang, K., Yu, X., Kwon, E. and Ou, J. (2012). "Electrical characteristics and pressure-sensitive response measurements of carboxyl MWNT/cement composites." *Cement and Concrete Composites*, Vol. 34, No. 6, pp. 794-800. doi: 10.1016/j.cemconcomp.2012.02.012.

Hou, T. C. and Lynch, J. P. (2005). "Conductivity-based strain monitoring and damage characterization of fiber reinforced cementitious structural components." Smart Structures and Materials, pp. 419-429.

Kim, D. J., El-Tawil, S. and Naaman, A. (2010). "Effect of matrix strength on pullout behavior of high-strength deformed steel fibers." Vol. 272, *ACI special publication*, pp. 135-150.

Kim, M. K. and Kim, D. J. (2018). "Electro-mechanical self-sensing response of ultra-high-performance fiber-reinforced concrete in tension Electromechanical response of high performance fiber reinforced cementitinous composites containing milled glass fibers under tension." *Materials*, Vol. 11, No. 7, pp. 1-18.

Kim, M. K., Kim, D. J. and An, Y. K. (2018). "Electro-mechanical self-sensing response of ultra-high-performance fiber-reinforced concrete in tension." *Composites Part B: Engineering*, Vol. 134, pp. 254-264. doi: 10.1016/j.compositesb.2017.09.061.

Le, H. V. and Kim, D. J. (2017). "Effect of matrix cracking on electrical resistivity of high performance fiber reinforced cementitious composites in tension." *Construction and Building Materials*, Vol. 156, pp. 750-760. doi: 10.1016/j.conbuildmat.2017.09.046.

Le, H. V., Moon, D. and Kim, D. J. (2018). "Effects of ageing and storage conditions on the interfacial bond strength of steel fibers in mortars." *Construction and Building Materials*, Vol. 170, pp. 129-141.

Lee, Y., Kang, S. T. and Kim, J. K. (2010). "Pullout behavior of inclined steel fiber in an ultra high strength cementitious matrix."

Construction and Building Materials, Vol. 24, No. 10, pp. 2030-2041.

Naaman, A. E. and Najm, H. (1991). "Bond-slip mechanisms of steel fibers in concrete." *ACI Materials Journal*, Vol. 88, No. 2, pp. 135-145.

Nguyen, D. L., Song, J., Manathamsombat, C. and Kim, D. J. (2014). "Comparative electromechanical damage-sensing behaviors of six strain-hardening steel fiber-reinforced cementitious composites under direct tension." *Composites Part B: Engineering*, Vol. 69, pp. 159-168. doi: 10.1016/j.compositesb.2014.09.037.

Park, S. H., Ryu, G. S., Koh, K. T. and Kim, D. J. (2014). "Effect of shrinkage reducing agent on pullout resistance of high-strength steel fibers embedded in ultra-high-performance concrete." *Cement and Concrete Composites*, Vol. 49, pp. 59-69. doi: 10.1016/j.cemconcomp.2013.12.012.

Peled, A., Torrents, J. M., Mason, T. O., Shah, S. P. and Garboczi, E. J. (2001). "Electrical impedance spectra to monitor damage during tensile loading of cement composites." *ACI Materials Journal*, Vol. 98, No. 4, pp. 313-322. doi: 10.14359/10400.

Pour-Ghaz, M., Kim, J., Nadukuru, S. S., Connor, S. M., Michalowski, R. L., Bradshaw, A., Green, R. A., Lynch, J. P., Poursaee, A. and Weiss, W. J. (2011). "Using electrical, magnetic and acoustic sensors to detect damage in segmental concrete pipes subjected to permanent ground displacement." *Cement & Concrete Composites*, Vol. 33, pp. 749-762.

Ranade, R., Zhang, J., Lynch, J. P. and Li, V. C. (2014). "Influence of micro-cracking on the composite resistivity of Engineered Cementitious Composites." *Cement and Concrete Research*, Vol. 58, pp. 1-12. doi: 10.1016/j.cemconres.2014.01.002.

Shannag, M. J., Brincker, R. and Hansen, W. (1997). "Pullout behavior of steel fibers from cement-based composites." *Cement and Concrete Research*, Vol. 27, No. 6, pp. 925-936. doi: 10.1016/S0008-8846(97)00061-6.

Shi, Z. Q. and Chung, D. D. L. (1999). "Carbon fiber-reinforced concrete for traffic monitoring and weighing in motion." *Cement and Concrete Research*, Vol. 29, No. 3, pp. 435-439. doi: 10.1016/S0008-8846(98)00204-X.

Song, J., Nguyen, D. L., Manathamsombat, C. and Kim, D. J. (2015). "Effect of fiber volume content on electromechanical behavior of strain-hardening steel-fiber-reinforced cementitious composites." *Journal of Composite Materials*, Vol. 49, No. 29, pp. 3621-3634. doi: 10.1177/0021998314568169.

Suryanto, B., McCarter, W. J., Starrs, G. and Ludford-jones, G. V. (2016). "Electrochemical immittance spectroscopy applied to a hybrid PVA/steel fiber engineered cementitious composite." *Materials and Design*, Vol. 105, No. 5, pp. 179-189. doi: 10.1016/j.matdes.2016.05.037.

Torrents, J. M., Mason, T. O. and Garboczi, E. J. (2000). "Impedance spectra of fiber-reinforced cement-based composites: A modeling approach." *Cement and Concrete Research*, Vol. 30, No. 4, pp. 585-592. doi: 10.1016/S0008-8846(00)00211-8.

Wang, D., Shi, C., Wu, Z., Xiao J., Huang, Z. and Fang, Z. (2015). "A review on ultra high performance concrete: Part II. Hydration, microstructure and properties." *Construction and Building Materials*, Vol. 96, pp. 368-377. doi: 10.1016/j.conbuildmat.2015.08.095.

Wen, S. and Chung, D. D. L. (2003). "A comparative study of steel- and carbon-fiber cement as piezoresistive strain sensors." *Advances in Cement Research*, Vol. 15, No. 3, pp. 119-128.

Wu, Z., Khayat, K. H. and Shi, C. (2018). "How do fiber shape and matrix composition affect fiber pullout behavior and flexural properties of UHPC?." *Cement and Concrete Composites*, Vol. 90, pp. 193-201. doi: 10.1016/j.cemconcomp.2018.03.021.

Yoo, D. Y., You, I. and Lee, S. J. (2017). "Electrical properties of cement-based composites with carbon nanotubes, graphene, and graphite nanofibers." *Sensors*, Vol. 17 No. 5, pp. 1-13. doi: 10.3390/s17051064.